Composites

Synthesis of KNbO$_3$/g-C$_3$N$_4$ composite and its new application in photocatalytic H$_2$ generation under visible light irradiation

Jinxiong Yu[1], Zhiqiang Chen[1], Yan Wang[4], Yuyin Ma[1], Zhe Feng[1], Hongjun Lin[3], Ying Wu[2], Leihong Zhao[2], and Yiming He[1,*]

[1] Department of Materials Science and Engineering, Zhejiang Normal University, Jinhua 321004, China

[2] Institute of Physical Chemistry, Zhejiang Normal University, Jinhua 321004, China

[3] College of Geography and Environmental Sciences, Zhejiang Normal University, Jinhua 321004, China

[4] Department of Chemical and Biological Engineering, Colorado School of Mines, Golden, CO 80401, USA

ABSTRACT

High-performance KNbO$_3$/g-C$_3$N$_4$ composite was prepared via a feasible method and first applied in photocatalytic H$_2$ production from water–methanol solution under irradiation of visible light. The structure and optical property of the synthesized composite were investigated by various techniques, including XRD, XPS, FT-IR, TEM, SEM, DRS, PL, and an electrochemical method. Results indicated that the combining of KNbO$_3$ with g-C$_3$N$_4$ did not affect the optical absorption. However, strong interaction between the two semiconductors was observed, which promotes the fabrication of a heterojunction structure and subsequently improves the separation of photogenerated electrons and holes. Hence, KNbO$_3$/g-C$_3$N$_4$ photocatalyst displayed obviously higher photoactivity than pristine g-C$_3$N$_4$. The photocatalytic hydrogen production rate for the optimal KNbO$_3$/g-C$_3$N$_4$ composite (7.4 wt% KNbO$_3$/g-C$_3$N$_4$) is 180 μmol g$_{cat}^{-1}$ h^{-1}, which is about 3.0 times that of pristine g-C$_3$N$_4$. Cycling tests further proved that KNbO$_3$/g-C$_3$N$_4$ showed good photocatalytic stability. Additionally, the effect of hole sacrificial agent on the photocatalytic activity was also investigated. The KNbO$_3$/g-C$_3$N$_4$ sample showed better performance in the presence of methanol than triethanolamine or EDTA-Na.

Address correspondence to E-mail: hym@zjnu.cn

🙋 Springer

Introduction

The critical environmental problem (greenhouse effect) throughout the world due to the utilization of fossil fuels requires a major restructuring of the energy system to reduce CO_2 emissions. The use of hydrogen as energy carriers is considered as one of the ideal options. Therefore, converting solar energy into hydrogen energy as an encouraging approach attracts scientists' attention. Since the innovative work of photocatalytic water decomposition on TiO_2 electrode was first reported by Honda and Fujishima in 1972 [1], great efforts have been devoted to developing high-efficiency photocatalysts to realize hydrogen production from water splitting. TiO_2 is the most popular photocatalyst because of its low expense, nontoxicity, and high stability. However, the photocatalytic hydrogen production on bare TiO_2 is limited due to its intrinsic wide band gap and fast recombination of photoexcited charge carriers. To conquer the bottleneck, many feasible methods including metal or nonmetal ion doping [2–4], noble metal loading [5, 6], dye sensitization [7], and semiconductor decoration [8, 9] have been developed. In particular, coupling a semiconductor with another narrow-band gap semiconductor greatly improves the photocatalytic H_2 generation of TiO_2. It is because a heterojunction structure is usually formed between TiO_2 and the combined semiconductor. The electron transfer in the heterojunction can improve both the optical performance and the separation of charge carriers, thus enhancing the photocatalytic activity. Additionally, this approach has been proven to be efficient in developing non-TiO_2-based photocatalysts [10–15], such as $ZnWO_4/WO_3$ [10], $Bi_2O_3/CaBi_6O_{10}$ [11], and $AgBr/Ag_3PO_4$ [13].

Potassium niobate ($KNbO_3$) is a perovskite oxide with promising application in nonlinear optical and electro-optical devices due to its large nonlinear susceptibility and high photorefractive coefficient. Meanwhile, $KNbO_3$ is also considered as a good photocatalyst for photocatalytic H_2 generation from water decomposition and has attracted lots of interest [16, 17]. For example, Zhang et al. [18] prepared cubic, orthorhombic, and tetragonal microcubes via hydrothermal method and investigated their photoreactivity in hydrogen production from methanol solution. It is found out that the photoactivity follows the orders: cubic > orthorhombic > tetragonal. Wang

et al. [19] investigated the photocatalytic hydrogen generation of $KNbO_3$ with different morphology under UV light. Similar work was also reported by Jiang et al. [20]. It should be noted that the above photocatalytic reactions are performed under UV light due to the wide band gap of $KNbO_3$. Similar to TiO_2, modification of $KNbO_3$ to extend the light absorption range is desired. However, few literatures about this topic have been reported so far [19, 21–23], especially on the $KNbO_3$-based composite photocatalyst. As far as we concerned, the extremely negative conduction band bottom of $KNbO_3$ may be the reason. It is reported that the CB bottom of $KNbO_3$ is estimated to be − 0.81 eV [24], which is much more negative than that of TiO_2 (− 0.35 eV) [8]. In other words, the semiconductor that can sensitize TiO_2 does not necessarily work on the $KNbO_3$-based composite system. Only a few semiconductors that have a high CB bottom may sensitize $KNbO_3$.

As the most stable allotrope of carbon nitride, polymeric g-C_3N_4 possesses a band gap of approximately 2.70 eV, indicating its property of visible light responsive (VLR). Wang et al. [25] first found that g-C_3N_4 can be a novel photocatalyst in hydrogen generation from water splitting. Since that, g-C_3N_4 as an effectual VLR photocatalyst has receiving considerable attention in the field of hydrogen generation [26, 27], CO_2 reduction [28, 29], and water purification [30, 31]. Meanwhile, g-C_3N_4 also has the property to act as the cocatalyst to sensitize other semiconductors. Due to the extremely negative CB bottom (− 1.20 eV), g-C_3N_4 can sensitize nearly all semiconductors, including $KTaO_3$ [32], $NaNbO_3$ [33], and YVO_4 [34], which may be the reason that different types of g-C_3N_4-based photocatalysts have been reported [35–42]. Additionally, the special characteristics indicate that g-C_3N_4 may be an ideal option to sensitize $KNbO_3$ photocatalyst. Actually, this approach has recently verified to be feasible by Shi et al. [24]. They prepared $KNbO_3$/g-C_3N_4 composite and investigated its photocatalytic activity in CO_2 reduction under visible light. However, the composite has never been applied to photocatalytic H_2 production. Considering the significance of the photocatalytic reaction, this research still deserves to be performed. Therefore, $KNbO_3$/g-C_3N_4 composite was prepared at a low temperature and initiatively applied to photocatalytic hydrogen generation under irradiation of visible light. The test result suggests that the $KNbO_3$/g-C_3N_4 composite presents high

photocatalytic hydrogen generation rate and stability. The effect of $KNbO_3$ concentration and the hole sacrificial agents on the performance of the photocatalyst was also evaluated.

Experimental part

Synthesis of photocatalysts

$g-C_3N_4$ was prepared by directing heating melamine in air atmosphere. Typically, 10 g melaimine was put in a semi-closed alumina crucible with a cover. Then, the crucible was moved into a muffle furnace and heated to 520 °C with a rate of 10 °C/min. After calcined at 520 °C for 4 h, the crucible was cooled naturally to room temperature. Yellow $g-C_3N_4$ powders were thus obtained.

$KNbO_3$ microcubes were synthesized as follows: 5.313 g Nb_2O_5 was added into 70 ml KOH solution (14 M) and stirred for an hour at room temperature. Then, the suspension was moved into a Teflon-lined steel autoclave ($V = 100$ mL). The autoclave was maintained at 160 °C for 12 h and then naturally cooled to room temperature. $KNbO_3$ white powders were finally obtained via centrifugation, washed with deionized water, and dried at 60 °C.

The $KNbO_3/g-C_3N_4$ composites were synthesized without the protection of any inert gas. $KNbO_3$ microcubes and $g-C_3N_4$ with various weight ratios were firstly mixed and ground in a motor for 30 min. The obtained powders were then heated to 350 °C with a rate of 10 °C/min. After thermal treatment at this temperature for 2 h, the muffle furnace containing the composite was cooled down to obtain $KNbO_3/g-C_3N_4$ hybrids with different $KNbO_3$ contents. To make it clear, the x wt% $KNbO_3/g-C_3N_4$ composites are denoted as x wt% KNCN, where x represents the mass concentration of $KNbO_3$.

Photocatalytic test

The photocatalytic H_2 production reactions of the $KNbO_3/g-C_3N_4$ composites were performed in a closed gas circulation system (Labsolar-IIIAI photocatalytic system, Beijing Perfectlight Co., Ltd., China, Figure S1). Typically, 100 mg of photocatalyst powders were dispersed in 100 mL water–methanol aqueous solution, which consists of 80 mL water and 20 ml CH_3OH. Methanol is used as the sacrificial agent. Then, 1 mL H_2PtCl_6 solution (0.002 M) was added. During the photocatalytic reaction, platinum (Pt) cocatalyst was deposited onto the photocatalyst samples in situ. The weight concentration of Pt was calculated to be 0.37 wt% of the added photocatalyst. The visible light source is a 300 W Xe lamp (PLS-SXE300C, Beijing ProfectLight Co. Ltd., China) equipped with a 420 nm cutoff filter. Prior to irradiation, the air in the reaction system was completely removed via a vacuum pump. The pressure is about 1.3 kPa. During the photocatalytic reaction, the pressure would be increased to about 6.3 kPa due to the production of H_2 and the evaporation of methanol. The concentration of the generated H_2 was analyzed every 30 min using an online gas chromatography (GC 7900, Shanghai Techcomp Instrument Ltd.) equipped with a thermal conductivity detector. The H_2 evolution reaction was also performed in the presence of EDTA-Na or triethanolamine (TEOA). When TEOA was used as the sacrificial agent, the amount (20 mL) is as same as the methanol. For EDTA-Na, the amount is controlled to be 0.01 mol with 100 mL water.

Characterizations of photocatalysts

Thermo-gravimetric (TG) profiles of the photocatalysts were obtained via a thermal analyzer (Netzsch STA449) in air flow (10 mL/min). The powder X-ray diffraction (XRD) analysis was performed on a Philips PW3040/60 X-ray diffractometer with Cu Kα radiation (40 kV/40 mA). Fourier transform-infrared (FT-IR) analyses were carried out on a Nicolet Nexus670 FT-IR spectrometer using KBr as the reference sample. Scanning electron microscopy (SEM) and energy-dispersive X-ray spectroscopy (EDS) images were collected on a field emission scanning electron microscope (Hitachi S-4800). Transmission electron microscopy (TEM) image was recorded with a JEM-2010F transmission electron microscope. UV–Visible diffuse reflection spectroscopy (DRS) was carried out on a UV–Visible spectrophotometer (PerkinElmer Lambda900) with $BaSO_4$ as reference sample. X-ray photoelectron spectroscopy (XPS) analyses were carried out in a Quantum 2000 Scanning ESCA Microprobe instrument using Al Kα. The photoluminescence (PL) analysis was performed on an FLS-920 spectrometer (Edinburgh Instrument), using a Xe lamp (excitation at 365 nm) as the light source. The electrochemical impedance spectroscopy

(EIS) and transient photocurrent (PC) analyses were carried out by using an Autolab electrochemical workstation with a standard three-electrode cell. The photocatalyst-coated ITO glass, Ag/AgCl, and Pt electrodes acted as the working, the reference, and the counter electrodes, respectively. The preparation of the working electrode is referred to the previous literature [42]. The electrolyte is 0.5 M Na_2SO_4 solution. A 300 W Xe lamp was used as the light source during the PC analysis.

Results and discussion

Characteristics of $KNbO_3$/g-C_3N_4 composites

Due to the weak thermal stability of g-C_3N_4 at high temperatures, the g-C_3N_4 concentration of g-C_3N_4-based composite photocatalyst usually changes during the preparation process. Therefore, TG analysis was performed to reveal the real g-C_3N_4 concentration in $KNbO_3$/g-C_3N_4 composite, and the result is shown in Fig. 1. All the photocatalysts have a significant weight loss due to the decomposition of g-C_3N_4. The temperature of the weight loss begins at about 500 °C for pure g-C_3N_4. For $KNbO_3$/g-C_3N_4 composite, the decomposition temperature is close to that of g-C_3N_4, indicating that unlike $SmVO_4$ or CeO_2, $KNbO_3$ does not significantly promote the decomposition of g-C_3N_4 [43, 44]. The weak oxidation ability of $KNbO_3$ may be the reason. The $KNbO_3$ concentration in the composite is determined based
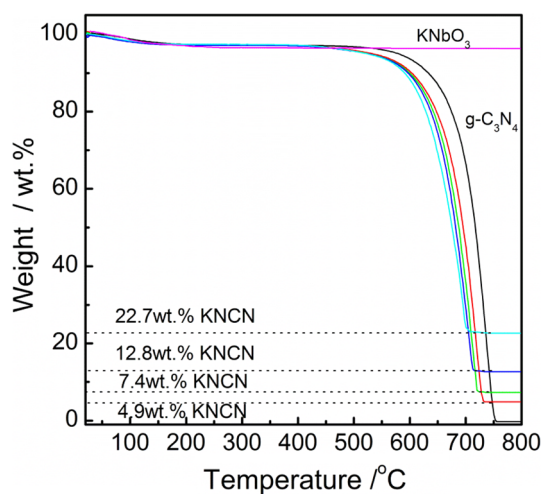

Fig. 2 XRD patterns of $KNbO_3$, g-C_3N_4, and $KNbO_3$/g-C_3N_4 composites.

upon the residual weight. The synthesized $KNbO_3$/g-C_3N_4 composites contain 4.9, 7.4, 12.8, and 22.7 wt% of $KNbO_3$, respectively.

The structure of $KNbO_3$/g-C_3N_4 composite was investigated by FT-IR and XRD. Figure 2 shows the XRD patterns of $KNbO_3$/g-C_3N_4 composites with various $KNbO_3$ concentrations. Pure g-C_3N_4 shows two characteristic signals at 13.1° and 27.4°, corresponding to the (001) plane associated with stacking layer and the (002) plane due to the assembling of the conjugated aromatic system, respectively [45]. The diffraction patterns of pure $KNbO_3$ can be assigned to orthorhombic $KNbO_3$ (PDF# 32-0822). The peaks at 22.1°, 31.5°, 45.2°, 50.9°, 56.0°, 65.8° can be indexed to (110), (111), (002), (221), (311), (222) diffraction planes, respectively. The $KNbO_3$/g-C_3N_4 composite presents both characteristic peaks of $KNbO_3$ and g-C_3N_4. With increasing $KNbO_3$ concentration, the intensities of the $KNbO_3$ diffraction peaks increase, whereas those of g-C_3N_4 decrease. No new phase is observed in the XRD patterns of $KNbO_3$/g-C_3N_4 composites, indicating the coupling of g-C_3N_4 and $KNbO_3$ does not cause any phase change.

Figure 3 shows the FT-IR spectra of $KNbO_3$/g-C_3N_4 composites. A series of absorption peaks in the range of 1200–1700 cm^{-1} are observed in the FT-IR spectrum of g-C_3N_4. These signals can be attributed to the typical stretching modes of C–N heterocycles [45, 46]. Additionally, another strong peak at 808 cm^{-1} associated with the breathing vibration of triazine units is also detected [45, 46]. For pure
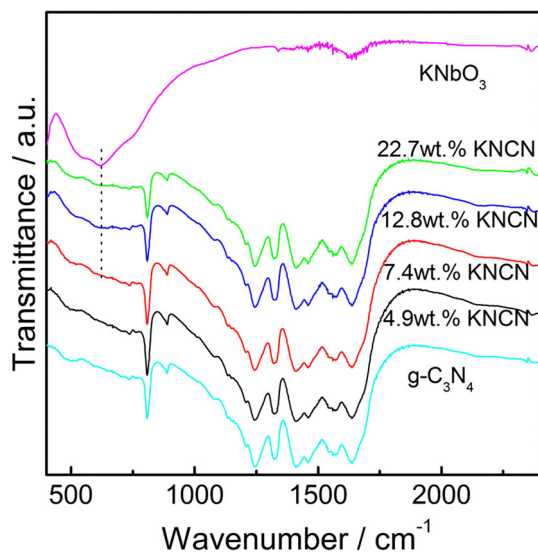

Fig. 1 TG Profiles of $KNbO_3$/g-C_3N_4 composites.

Fig. 3 FT-IR spectra of $KNbO_3/g-C_3N_4$ composite with various $KNbO_3$ concentration.

$KNbO_3$, there is a broad and strong band at about 610 cm^{-1}, corresponding to the characteristic vibration of Nb–O octahedron [47]. The FT-IR spectra of $KNbO_3/g-C_3N_4$ are nearly the same as those of $g-C_3N_4$. But for the samples with high $KNbO_3$ content, the characteristic peak of $KNbO_3$ at about 610 cm^{-1} can also be observed, indicating the hybrid structure, which accords well with the XRD experiment.

The elemental composition and chemical status of $KNbO_3/g-C_3N_4$ were analyzed by XPS. Figure 4a shows the conspectus spectra of $KNbO_3$, $g-C_3N_4$, and a representative $KNbO_3/g-C_3N_4$ composite (7.4 wt% KNCN). It can be seen from the figure that all the elements of K, Nb, C, N, and O are observed in the 7.4 wt % KNCN composite, while $g-C_3N_4$ and $KNbO_3$ consist of C, N and K, Nb, O elements, respectively. The C1s spectrum of $g-C_3N_4$ in Fig. 4b displays two distinct peaks at 284.6 eV and 287.8 eV, respectively. The first peak is assigned to sp^2-hybridized carbon atoms in graphitic domains, which originates from the adventitious carbon [48, 49]. This carbon peak can be observed in all samples. The second peak results from carbon atom bonded with three nitrogen atoms in the $g-C_3N_4$ lattice [48]. Only the sample containing $g-C_3N_4$ shows this C1s peak. Meanwhile, compared with pristine $g-C_3N_4$, a slightly positive shift of the C1s peak is observed with the $KNbO_3/g-C_3N_4$ photocatalyst, suggesting the interaction between $KNbO_3$ and $g-C_3N_4$ phases, which results in the change of the

chemical surrounding of $g-C_3N_4$. This phenomenon also appears in the XPS spectra of N1s and Nb3d. A slightly positive shift is observed in the N1s XPS spectrum of $KNbO_3/g-C_3N_4$ sample. For Nb3d spectrum, it shows a slightly negative shift. A possible explanation for this phenomenon is the electron migration from the electron-rich $g-C_3N_4$ to $KNbO_3$, resulting in the enhanced electron density of $KNbO_3$ [36, 50]. Figure 4d shows the O1s XPS spectra of $KNbO_3$, $g-C_3N_4$, and 7.4 wt% KNCN. $KNbO_3$ sample shows a strong O1s peak at 529.1 eV, corresponding to the lattice oxygen of $KNbO_3$. The O1s peak of $g-C_3N_4$ locates at 532.4 eV, which originates from the oxygen in OH group or adsorbed H_2O species [51]. The $KNbO_3/g-C_3N_4$ sample displays a similar O1s spectrum to that of $g-C_3N_4$ due to the high concentration of $g-C_3N_4$. Meanwhile, it can also be observed that the existence of $KNbO_3$ phase leads to a slightly negative shift of the O1s peak. Clearly, all above analyses confirm the successful preparation of $KNbO_3/g-C_3N_4$ composite, rather than a physical mixture of $g-C_3N_4$ and $KNbO_3$. Meanwhile, the interface energy can be decreased via the interaction between $KNbO_3$ and $g-C_3N_4$, which favors the electron migration at the interface of the two semiconductors. The element composition of 7.4 wt % $KNbO_3/g-C_3N_4$ is also estimated based on the XPS peak area and the corresponding correction factors. The atomic ratio of C:N:K:Nb is calculated to be 1:1.32:0.25:0.20. Considering that the theoretical value is 1:1.33:0.04:0.04, it can be deduced that the surface concentration of $KNbO_3$ is lower than the volume value. This phenomenon may be attributed to that the $KNbO_3$ microcube is usually covered by $g-C_3N_4$ particles, just as shown in the SEM image (Fig. 5d). Figure 4f demonstrates the VB XPS spectra of $KNbO_3$ and $g-C_3N_4$. The VB edge potentials of $g-C_3N_4$ and $KNbO_3$ are determined to be 1.50 and 2.16 eV, respectively. Both are consistent with the previous results [24, 33].

The morphology and microstructure of $KNbO_3/g-C_3N_4$ are investigated via SEM and TEM. Pure $g-C_3N_4$ is composed of small particles and shows an irregular shape, while $KNbO_3$ shows the morphology of microcube with an average size of 2–3 μm (Fig. 5a, b). Figure 5c and d exhibits the SEM photographs of $KNbO_3/g-C_3N_4$ composite. Both $KNbO_3$ and $g-C_3N_4$ can be easily observed due to their different morphology. It can be seen that $KNbO_3$ microcubes disperse in the $g-C_3N_4$ and small $g-C_3N_4$ particles are
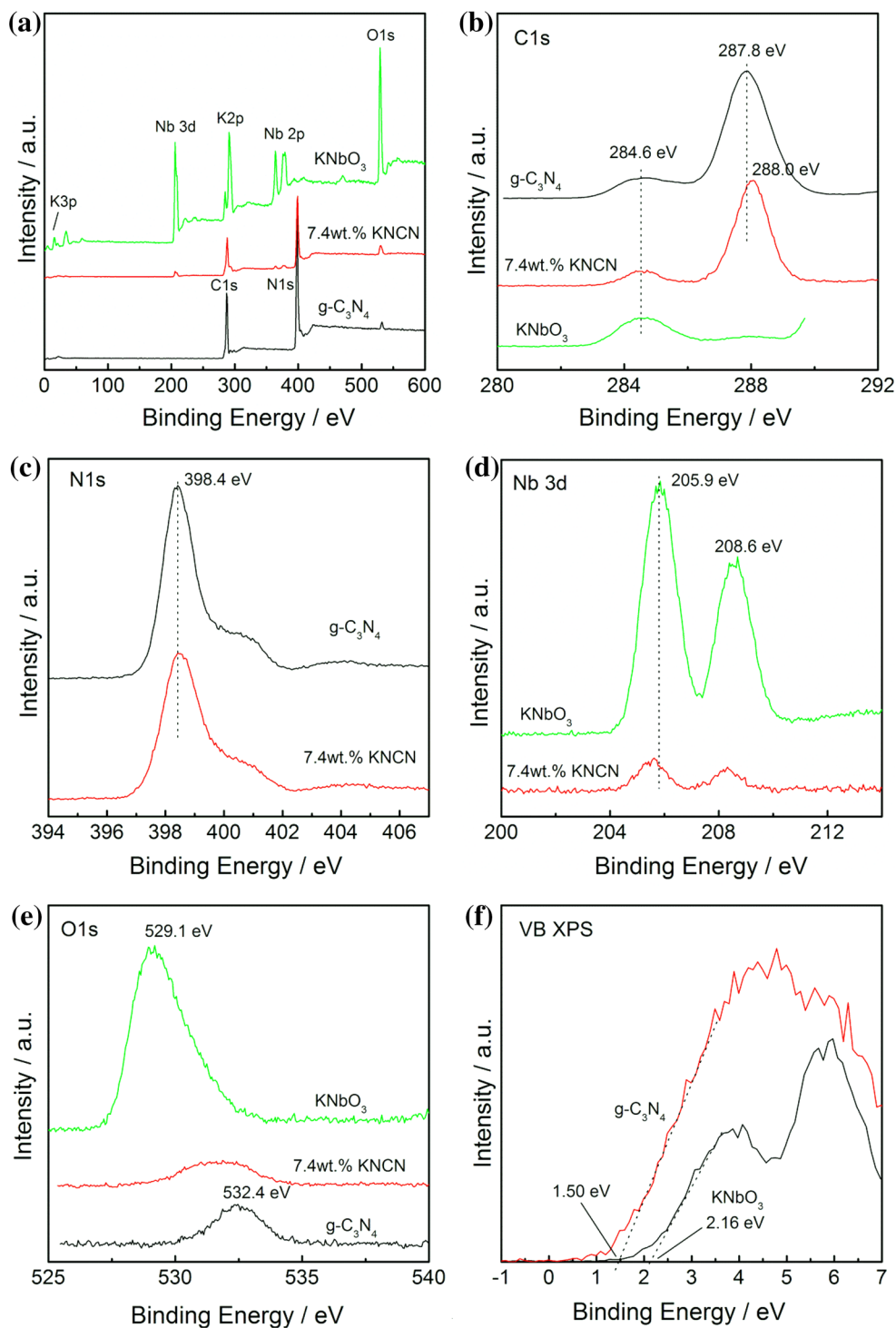
Fig. 4 XPS spectra of pure g-C_3N_4, $KNbO_3$, $KNbO_3$/g-C_3N_4 composite. **a** survey XPS spectra; **b** C1s; (c) N1s; **d** Nb3d; **e** O1s; **f** VB XPS.

decorated on the $KNbO_3$ surface. This result is further confirmed via EDS analysis. As shown in Fig. 5e, all the elements of C, N, O, K, Nb are detected, indicating the hybrid structure of $KNbO_3$/g-C_3N_4.

The detected contents of K and Nb are higher than those of C and N, which is probably due to that the detected region lies on a $KNbO_3$ microcube (Fig. 5d). Figure 5f displays the TEM image of $KNbO_3$/g-C_3N_4

Fig. 5 SEM image of g-C$_3$N$_4$ (**a**), KNbO$_3$ (**b**) and KNbO$_3$/g-C$_3$N$_4$ composite (**c**, **d**), EDS result (**e**), and TEM image (**f**) of KNbO$_3$/g-C$_3$N$_4$ composite.
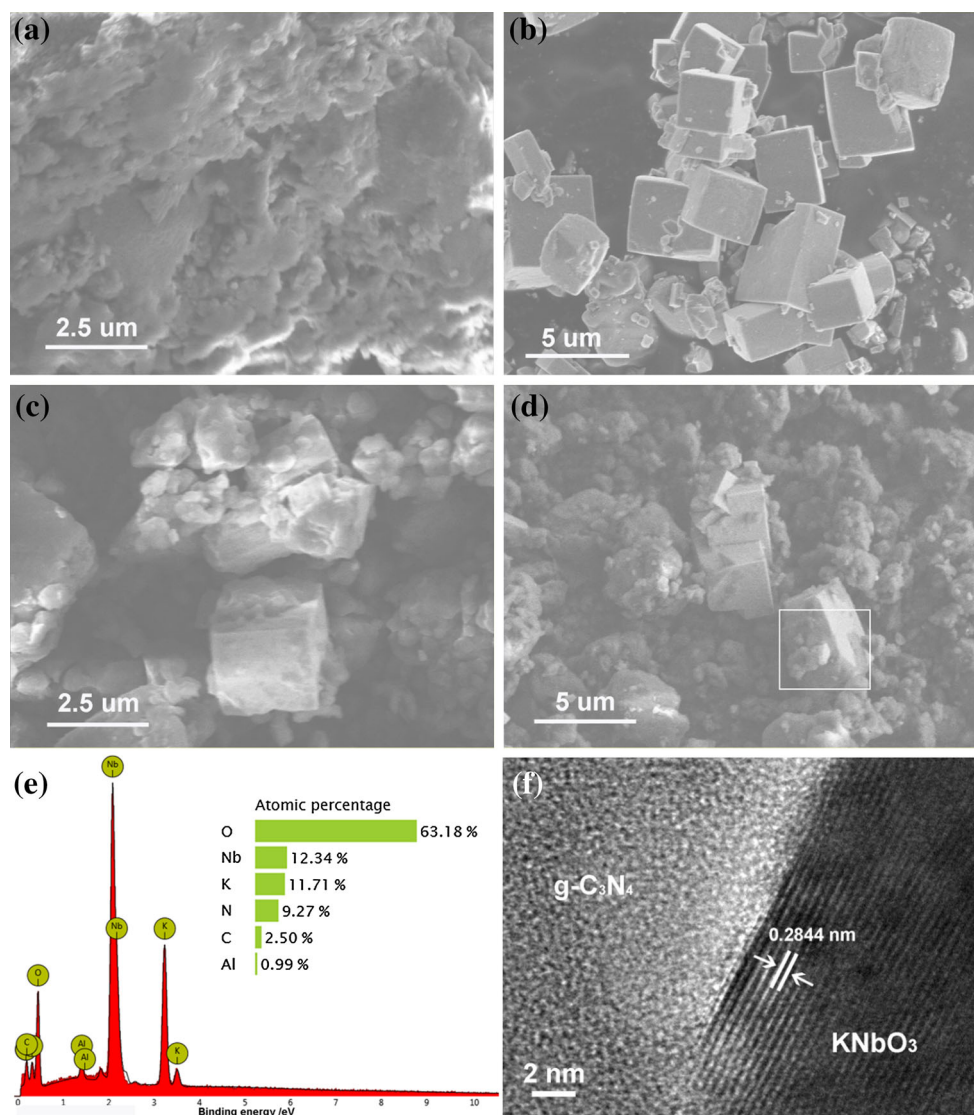
composite. The light color part can be ascribed to g-C$_3$N$_4$ phase, while the dark part is KNbO$_3$ based on their different atomic weight. Meanwhile, the dark part shows a clear lattice fringe of 0.2808 nm, which corresponds to the (111) plane of KNbO$_3$. For g-C$_3$N$_4$, no lattice fringe is observed due to its weak crystallinity [33]. Anyway, the TEM analysis proves that g-C$_3$N$_4$ is closely decorated on the KNbO$_3$ surface. The observed smooth and intimate interface is probably beneficial to the transfer of photoexcited charge carriers and thereby retards the recombination of electron–hole pairs [33, 52].

PL, EIS, and photocurrent response analyses were carried out to survey the separation efficiency of charge carriers in the synthesized KNbO$_3$/g-C$_3$N$_4$ photocatalyst. Figure 6 shows the PL spectra of g-C$_3$N$_4$, 7.4 wt% KNCN, and 7.4 wt% KNCN-PM (a physical mixture of KNbO$_3$ and g-C$_3$N$_4$). It can be seen that g-C$_3$N$_4$ and KNbO$_3$/g-C$_3$N$_4$ show a similar PL peak at approximately 460 nm, suggesting that the PL signal originates from g-C$_3$N$_4$ phase. However, the PL peak of 7.4 wt% KNCN is much weaker than that of g-C$_3$N$_4$. Considering that the PL signal comes from the recombination of photoexcited charge carriers, the data in Fig. 6 indicate that the introduction of KNbO$_3$ prevents the recombination of electrons and holes [34, 43], which process contributes to the photocatalytic process. The physical mixture of KNbO$_3$ and g-C$_3$N$_4$ was prepared as a reference sample to evaluate the effect of g-C$_3$N$_4$ content. The PL peak of the 7.4 wt% KNCN-PM is still higher than that of 7.4 wt% KNCN composite,
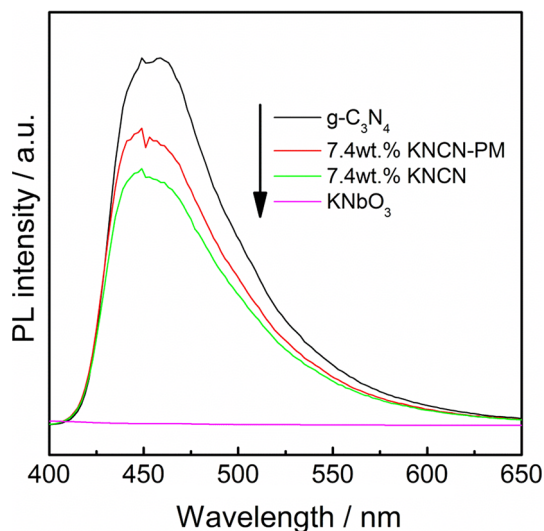
Fig. 6 PL spectra of g-C$_3$N$_4$, 7.4 wt % KNCN, and 7.4 wt % KNCN-PM.

which definitely proves that the decreased PL signal mainly results from the enhanced separation efficiency of charge carriers.

Besides PL technique, photocurrent response and EIS are also effective in evaluating the separation efficiency of charge carriers. Figure 7a displays the electrochemical impedance spectroscopy of KNbO$_3$, g-C$_3$N$_4$, and 7.4 wt% KNCN. In general, a smaller arc size means a lower charge transfer resistance on the surface of materials [50, 53]. The data in Fig. 7a display that the arc ratios of the three samples show the sequence: g-C$_3$N$_4$ > 7.4 wt% KNCN-PM ≈ KNbO$_3$ > 7.4 wt% KNCN. This result suggests that the KNbO$_3$/g-C$_3$N$_4$ composite has lower interfacial electron transfer resistance, which can promote electron transfer efficiency and subsequently results in a high separation efficiency of charge carriers. Meanwhile, this result indicates that no synergetic effect is observed in physical mixture of KNbO$_3$ and g-C$_3$N$_4$, which is consistent with the PL analysis. This conclusion is further confirmed by the photocurrent analysis. The photocurrent responses of the above four samples with several intermittent on–off cycles are shown in Fig. 7b. It can be observed that the KNbO$_3$/g-C$_3$N$_4$ composite presents much higher photocurrent compared with other samples, indicating that the composite holds stronger capability in inhibiting the recombination of electron–hole pairs than g-C$_3$N$_4$ [54, 55].

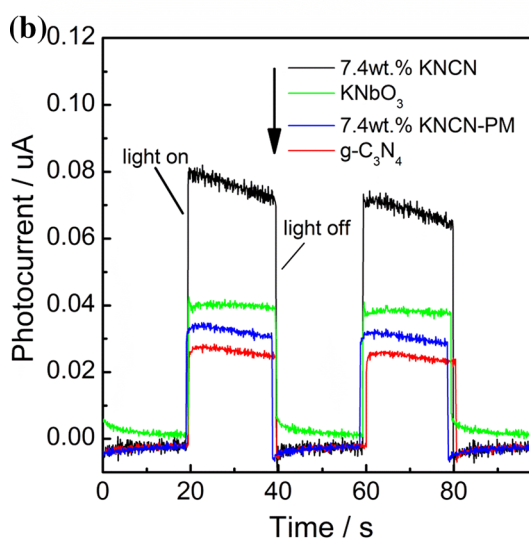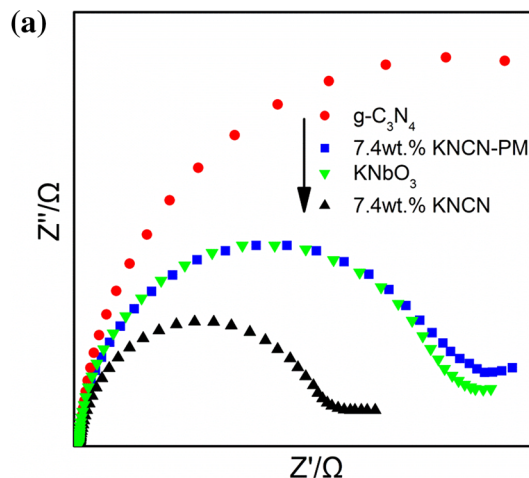UV–Vis spectra of KNbO$_3$, g-C$_3$N$_4$, and KNbO$_3$/g-C$_3$N$_4$ photocatalysts are measured and shown in

Fig. 7 EIS (a) and transient photocurrent responses (b) of g-C$_3$N$_4$, KNbO$_3$, 7.4 wt % KNCN, and 7.4 wt % KNCN-PM.
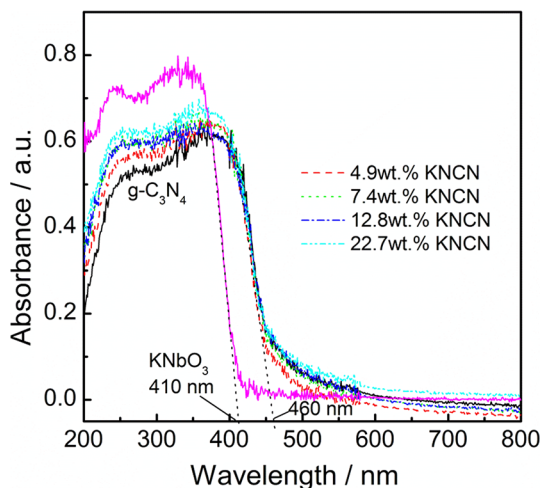

Fig. 8 UV–Vis spectra of KNbO$_3$/g-C$_3$N$_4$ composites.

Fig. 8. Pure $KNbO_3$ can only absorb UV light with a wavelength lower than 410 nm. The band gap energy is calculated to be 3.02 eV based on the equation of $E_g = 1240/\lambda$ [56]. G-C_3N_4 shows better capability in light absorption. The absorption threshold is determined to be 460 nm, corresponding to its band gap of 2.70 eV. Both accord well with the previous values [24, 33]. For $KNbO_3$/g-C_3N_4 composite, the combination of $KNbO_3$ with g-C_3N_4 promotes the absorption peak in the UV light region. However, the absorbance threshold is not changed, indicating that all the composites present nearly the same ability in absorbing visible light.

Photocatalytic H_2 production of $KNbO_3$/g-C_3N_4 composites

The catalytic performance of the synthesized $KNbO_3$/g-C_3N_4 composite was investigated via the photocatalytic H_2 generation under irradiation of visible light. Figure 9 displays the photocatalytic H_2 generation performance of $KNbO_3$, g-C_3N_4, and $KNbO_3$/g-C_3N_4 composite. Almost no H_2 is generated in the presence of pure $KNbO_3$, which is mainly ascribed to its wide band gap. Pure g-C_3N_4 holds a good response to visible light. Hence, it shows much better photocatalytic activity than $KNbO_3$, with a hydrogen production rate of 58.7 μmol g_{cat}^{-1} h^{-1}. The combination of $KNbO_3$ with g-C_3N_4 greatly promotes the photocatalytic performance. With increasing $KNbO_3$ concentration from 4.9 to 22.7 wt%, the catalytic performance of the photocatalyst enhances first
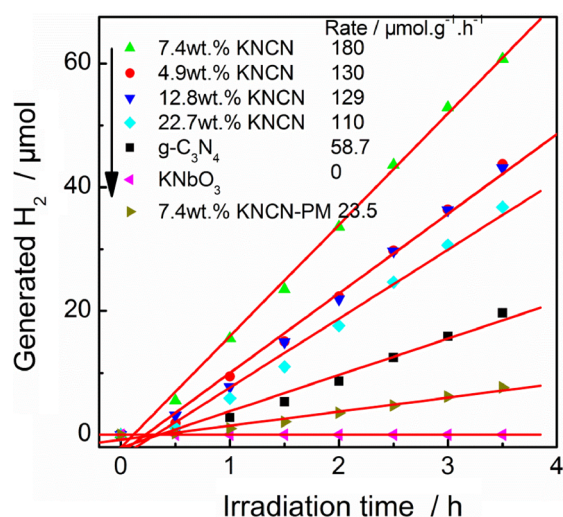
and then reduces. The sample with 7.4 wt% $KNbO_3$ presents the best photocatalytic performance. The photocatalytic hydrogen generation rate reaches 180 μmol g_{cat}^{-1} h^{-1}, which is 3.0 times higher than that of g-C_3N_4. Obviously, the coupling of $KNbO_3$ and g-C_3N_4 generates an efficient VLR photocatalyst for hydrogen generation from water–methanol solution, and the synergetic effect between the two phases may be the origin of the excellent photocatalytic performance. A powerful proof for the inference is the photocatalytic activity of the 7.4 wt% KNCN-PM sample. EIS and PC analyses have proven that no synergy effect exists in the sample, and the physical mixture presents worse ability in H_2 evolution (23.5 μmol g_{cat}^{-1} h^{-1}) than pure g-C_3N_4. The 7.4 wt% KNCN composite may have a suitable $KNbO_3$ content, which promotes the transport and separation of the electron–hole pairs with the proper distribution of $KNbO_3$ inside g-C_3N_4. At a higher concentration of $KNbO_3$, the microcubes may shield g-C_3N_4 and decrease the photocatalytic activity.

Figure 10 shows the cycling test of the 7.4 wt% KNCN composite in photocatalytic H_2 production. After performing the photocatalytic reaction in the methanol–water solution for 3.5 h, the generated hydrogen in the closed circulation system was completely removed for the next cycling test. As Fig. 10 shows, there is only slight decrease in the photocatalytic hydrogen generation rate, displaying a negligible reduction after the fourth run, and indicating the high steadiness of $KNbO_3$/g-C_3N_4 composite. The slight reduction in H_2 generation rate may be

Fig. 9 Photocatalytic hydrogen production performance of $KNbO_3$/g-C_3N_4 composite under irradiation of visible light.
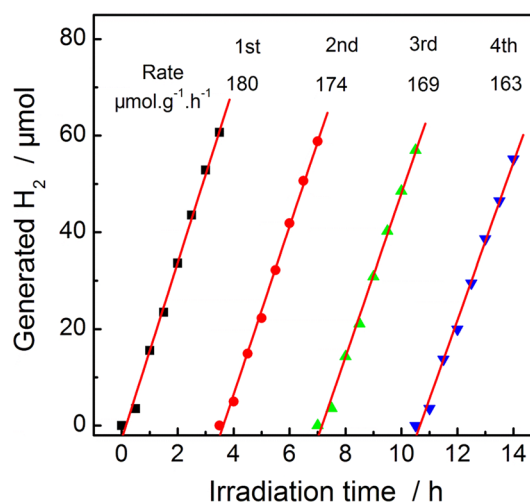

Fig. 10 Five-cycling test of 7.4 wt % KNCN composite sample in photocatalytic hydrogen production.

attributed to the consumption of methanol during the cycling test. This result also indicates the importance of the hole sacrificial agent. Therefore, another two common sacrificial agents, TEOA and EDTA-Na [57, 58], were also used to investigate the photocatalytic hydrogen production of 7.4 wt% KNCN, and the result is shown in Fig. 11. It indicates that the hydrogen generation rate is 150 $\mu mol\ g_{cat}^{-1}\ h^{-1}$ when methanol is replaced by TEOA as the hole sacrificial agent. For EDTA-Na, the rate significantly decreases to 38 $\mu mol\ g_{cat}^{-1}\ h^{-1}$. The KNbO$_3$/g-C$_3N_4$ shows the best H$_2$ production performance in the methanol–water solution. It is reported that methanol can also be the origin of the generated H$_2$ besides its role in eliminating holes [59]. Hence, it is deduced that the generated hydrogen comes from both methanol and water. Just like methanol, TEOA also has the functional group of –OH, which may be the reason that the 7.4 wt% KNCN shows a similar H$_2$ production rate in the presence of either methanol or TEOA. Different from methanol or TEOA, EDTA-Na has no –OH group, which results in its weak photocatalytic performance. However, there is no doubt that KNbO$_3$/g-C$_3$N$_4$ composite has the ability of photocatalytically split water into hydrogen base on the data in Fig. 11.

Discussion

The UV–Vis absorption has verified that the synthesized KNbO$_3$/g-C$_3$N$_4$ and g-C$_3$N$_4$ have similar photoabsorption performance, indicating that the

coupling of KNbO$_3$ does not affect the optical property of g-C$_3$N$_4$. However, the introduced KNbO$_3$ and g-C$_3$N$_4$ show a strong interaction, which leads to the enhanced segregation efficiency of electron–hole pairs, as proven by PL, EIS, and photocurrent response. The performance examination indicates that the introduction of KNbO$_3$ onto g-C$_3$N$_4$ greatly promotes the generation of H$_2$. Therefore, it is deduced that the efficient charge separation acts like a pivotal role in affecting its performance in photocatalytic reaction, just as other g-C$_3$N$_4$-based composite photocatalysts [32–44, 60, 61]. The band potentials of g-C$_3$N$_4$ and KNbO$_3$ were explored to clarify the separation of charge carriers in g-C$_3$N$_4$/KNbO$_3$ interfaces. Via the VB XPS analysis, the valence band top of g-C$_3$N$_4$ and KNbO$_3$ has been measured to be 1.50 and 2.16 eV, respectively. Based on the relationship between CB and VB ($E_{CB} = E_{VB} - E_g$), the conduction band bottoms of g-C$_3$N$_4$ and KNbO$_3$ are separately estimated to be -1.20 and -0.86 eV. Thus, it can be concluded that g-C$_3$N$_4$ has higher CB and VB than KNbO$_3$. The appropriate band potentials indicate that the two semiconductors can fabricate a heterojunction structure. Based on the aforementioned analysis and the reported literatures [32–44, 60, 61], a probable mechanism for the improved photocatalytic H$_2$ generation over the KNbO$_3$/g-C$_3$N$_4$ composite is illustrated in Fig. 12. Only g-C$_3$N$_4$ can be excited to produce electrons and holes under irradiation of visible light. Hence, g-C$_3$N$_4$ plays the role of a sensitizer to absorb light and
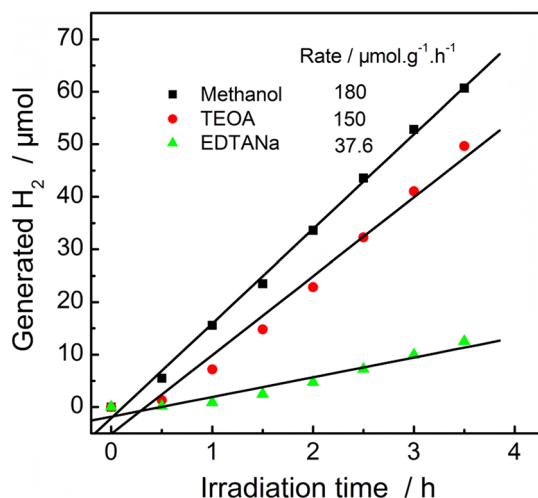

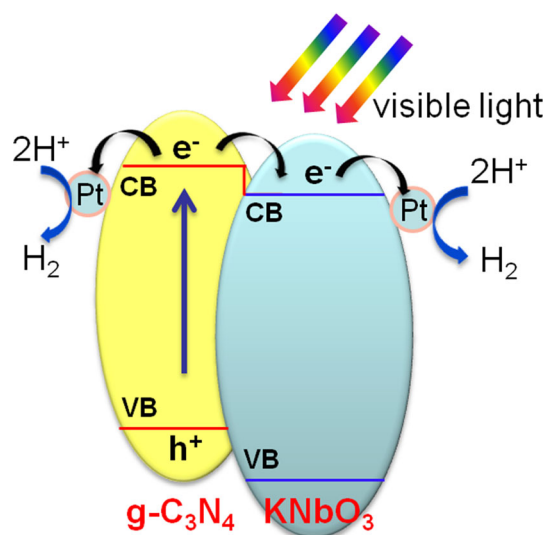**Fig. 11** Photocatalytic hydrogen production of 7.4 wt % KNCN sample in the presence of different hole sacrificial agents.

Fig. 12 Possible schemes for electron–hole separation and transport at the KNbO$_3$/g-C$_3$N$_4$ composite interface.

produce electrons in the heterojunction system. The photogenerated electrons on g-C_3N_4 can migrate to the CB of $KNbO_3$ driven by the potential difference of the two semiconductors. Then, the photoexcited electrons could be quickly transferred to the in situ loaded Pt to generate H_2 because metallic noble Pt can serve as an excellent electron acceptor. Through this scheme, the photoexcited electrons and holes are effectively divorced in the photocatalyst, and therefore, the photocatalytic hydrogen production rate is significantly enhanced.

Conclusion

In this study, a high-efficiency $KNbO_3/g$-C_3N_4 composite photocatalyst was developed and applied in photocatalytic H_2 generation in water–methanol solution with the help of metallic Pt. The developed $KNbO_3/g$-C_3N_4 composite presents much higher H_2 production rate than pure g-C_3N_4 or $KNbO_3$ under the irradiation of visible light. The improved photocatalytic performance is mostly attributed to the matched CB and VB of the $KNbO_3$ and g-C_3N_4, which leads to the efficient inhibition of the recombination of the photoexcited electron–hole pairs in the heterojunction system. This work may be a useful reference for the future design of g-C_3N_4-based photocatalyst in photocatalytic hydrogen generation.

Acknowledgements

Electronic supplementary material: The online version of this article (https://doi.org/10.1007/s10853-018-2119-5) contains supplementary material, which is available to authorized users.

References

[1] Fujishima A, Honda K (1972) Electrochemical photolysis of water at a semiconductor electrode. Nature 238:37–38

[2] Choi W, Termin A, Hoffmann MR (1994) The role of metal ion dopants in quantum-sized TiO_2: correlation between photoreactivity and charge carrier recombination dynamics. J Phys Chem 98:13669–13679

[3] LuoYJ XuYX, Liu XP, Xue H, Qian QR, Chen QH (2017) Design of Cu–Ce co-doped TiO_2 for improved photocatalysis. J Mater Sci 52:1265–1271. https://doi.org/10.1007/s10853-016-0421-7

[4] Nawawi WI, Nawi MA (2014) Carbon coated nitrogen doped P25 for the photocatalytic removal of organic pollutants under solar and low energy visible light irradiations. J Mol Catal A: Chem 383–384:83–93

[5] Bamwend GR, Tsubota S, Nakamura T, Haruta M (1995) Photoassisted hydrogen production from a water-ethanol solution: a comparison of activities of Au-TiO_2 and Pt-TiO_2. J Photochem Photobiol A: Chem 89:177–189

[6] Shet A, Vidya SK (2016) Solar light mediated photocatalytic degradation of phenol using Ag core–TiO_2 shell (Ag@TiO_2) nanoparticles in batch and fluidized bed reactor. Sol Energy 127:67–78

[7] Qin GH, Sun Z, Wu QP, Lin L, Liang M, Xue S (2011) Dye-sensitized TiO_2 film with bifunctionalized zones for photocatalytic degradation of 4-cholophenol. J Hazard Mater 192:599–604

[8] Liu MJ, He L, Liu XN, Liu CB, Luo SL (2014) Reduced graphene oxide and CdTe nanoparticles co-decorated TiO_2 nanotube array as a visible light photocatalyst. J Mater Sci 49:2263–2269. https://doi.org/10.1007/s10853-013-7922-4

[9] Daousa M, Iliev V, Petrovc L (2014) Gold-modified N-doped TiO_2 and N-doped WO_3/TiO_2 semiconductors as photocatalysts for UV–visible light destruction of aqueous 2,4,6-trinitrotoluene solution. J Mol Catal A: Chem 392:194–201

[10] Leonard KC, Nam KM, Lee HC, Kang SH, Park HS, Bard AJ (2013) $ZnWO_4/WO_3$ composite for improving photoelectrochemical water oxidation. J Phys Chem C 117:15901–15910

[11] Wang J, He YM, Li TT, Cai J, Luo MF, Zhao LH (2012) Photocatalytic degradation of methylene blue on $CaBi_6O_{10}/Bi_2O_3$ composites under visible light. Chem Eng J 189–190:473–481

[12] Iqbal N, Khan I, Yamani ZHA, Qurashi A (2017) A facile one-step strategy for in situ fabrication of WO_3–$BiVO_4$ nanoarrays for solar-driven photoelectrochemical water splitting applications. Sol Energy 144:604–644

[13] Cao J, Luo BD, Lin HL, Xu BY, Chen SF (2012) Visible light photocatalytic activity enhancement and mechanism of $AgBr/Ag_3PO_4$ hybrids for degradation of methyl orange. J Hazard Mater 217–218:107–115

[14] Cui M, Yu JX, Lin HJ, Wu Y, Zhao LH, He YM (2016) In-situ preparation of Z-scheme AgI/Bi_5O_7I hybrid and its excellent photocatalytic activity. Appl Surf Sci 387:912–920

[15] Yu JG, Zhang J, Jaroniec M (2010) Preparation and enhanced visible-light photocatalytic H_2-production activity of CdS quantum dots-sensitized $Zn_{1-x}Cd_xS$ solid solution. Green Chem 12:1611–1614

[16] Grabowska E (2016) Selected perovskite oxides: characterization, preparation and photocatalytic properties—a review. Appl Catal B: Environ 186:97–126

[17] Yan LS, Zhang J, Zhou XM, Wu XX, Lan JY, Wang YS, Liu G, Yu JG, Zhi LJ (2013) Crystalline phase-dependent photocatalytic water splitting for hydrogen generation on $KNbO_3$ submicro-crystals. Int J Hydrogen Energ 38:3554–3561

[18] Zhang TT, Zhao K, Yu JG, Jin J, Qi Y, Li HQ, Hou XJ, Liu G (2013) Photocatalytic water splitting for hydrogen generation on cubic, orthorhombic, and tetragonal $KNbO_3$ microcubes. Nanoscale 5:8375–8383

[19] Wang RW, Zhu YF, Qiu YF, Leung CF, He J, Liu GJ, Lau TC (2013) Synthesis of nitrogen-doped $KNbO_3$ nanocubes with high photocatalytic activity for water splitting and degradation of organic pollutants under visible light. Chem Eng J 226:123–130

[20] Jiang LQ, Qiu Y, Yi ZG (2013) Potassium niobate nanostructures: controllable morphology, growth mechanism, and photocatalytic activity. J Mater Chem A 1:2878–2885

[21] Choi J, Ryu SY, Balcerski W, Lee TK, Hoffmann MR (2008) Photocatalytic production of hydrogen on $Ni/NiO/KNbO_3/CdS$ nanocomposites using visible light. J Mater Chem 18:2371–2378

[22] Wang JQ, Wang X, Cui ZT, Liu B, Cao MH (2015) One-pot synthesis and Nb_4N_5 surface modification of Nb^{4+} self-doped $KNbO_3$ nanorods for enhanced visible-light-driven hydrogen production. Phys Chem Chem Phys 17:14185–14192

[23] Lan JY, Zhou XM, Liu G, Yu JG, Zhang JC, Zhi LJ, Nie GJ (2011) Enhancing photocatalytic activity of one-dimensional $KNbO_3$ nanowires by Au nanoparticles under ultraviolet and visible-light. Nanoscale 3:5161–5167

[24] Shi HF, Zhang CL, Zhou CP, Chen GQ (2015) Conversion of CO_2 into renewable fuel over $Pt–g-C_3N_4/KNbO_3$ composite photocatalyst. RSC Adv 5:93615–93622

[25] Wang XC, Maeda K, Thomas A, Takanabe K, Xin G, Domen K, Antonietti M (2009) A metal-free polymeric photocatalyst for hydrogen production from water under visible light. Nat Mater 8:76–80

[26] Hong JD, Xia XY, Wang YS, Xu R (2012) Mesoporous carbon nitride within situ sulfur doping for enhanced photocatalytic hydrogen evolution from water under visible light. J Mater Chem 22:15006–15012

[27] Schwinghammer K, Mesch MB, Duppel V, Ziegler C, Senker J, Lotsch BV (2014) Crystalline carbon nitride nanosheets for improved visible-light hydrogen evolution. J Am Chem Soc 136:1730–1733

[28] He YM, Wang Yan Zhang LH, Teng BT, Fan MH (2015) High-efficiency conversion of CO_2 to fuel over $ZnO/g-C_3N_4$ photocatalyst. Appl Catal B: Environ 168–169:1–8

[29] Lang QQ, Yang YJ, Zhu YZ, Hu WL, Jiang WY, Zhong SA, Gong PJ, Teng BT, Zhao LH, Bai S (2017) High-index facet engineering of PtCu cocatalysts for superior photocatalytic reduction of CO_2 to CH_4. J Mater Chem A 5:6686–6694

[30] Zhao HX, Yu HT, Quan X, Chen S, Zhao HM, Wang H (2014) Atomic single layer graphitic-C_3N_4: fabrication and its high photocatalytic performance under visible light irradiation. RSC Adv 4:624–628

[31] Tian YL, Chang BB, Lu JL, Fu J, Xi FN, Dong XP (2013) Hydrothermal synthesis of graphitic carbon nitride–Bi_2WO_6 heterojunctions with enhanced visible light photocatalytic activities. ACS Appl Mater Interfaces 5:7079–7085

[32] Yong ZQ, Ren J, Hu HL, Li P, Ouyang SX, Xu H, Wang DF (2015) Synthesis, characterization, and photocatalytic activity of $g-C_3N_4/KTaO_3$ composites under visible light irradiation. J Nanomater. Article ID: 821986

[33] Shi HF, Chen GQ, Zhang CL, Zou ZG (2014) Polymeric $g-C_3N_4$ coupled with $NaNbO_3$ nanowires toward enhanced photocatalytic reduction of CO_2 into renewable fuel. ACS Catal 4:3637–3643

[34] Cai J, He YM, Wang XX, Zhang LH, Dong LZ, Lin HJ, Zhao LH, Yi XD, Weng WZ, Wan HL (2013) Photodegradation of RhB over $YVO_4/g-C_3N_4$ composites under visible light irradiation. RSC Adv 3:20862–20868

[35] Habibi-Yangjeh A, Akhundi A (2016) Novel ternary $g-C_3N_4/Fe_3O_4/Ag_2CrO_4$ nanocomposites: magnetically separable and visible-light-driven photocatalysts for degradation of water pollutants. J Mol Catal A: Chem 415:122–130

[36] Yu JX, Nong QY, Jiang XL, Liu XZ, Wu Y, He YM (2016) Novel $Fe_2(MoO_4)_3/g-C_3N_4$ heterojunction for efficient contaminant removal and hydrogen production under visible light irradiation. Sol Energy 139:355–364

[37] He YM, Zhang LH, Teng BT, Fan MH (2015) A new application of Z-scheme $Ag_3PO_4/g-C_3N_4$ composite in converting CO_2 to fuel. Environ Sci Technol 49:649–656

[38] Mousavi M, Habibi-Yangjeh A (2016) Magnetically separable ternary $g-C_3N_4/Fe_3O_4/BiOI$ nanocomposites: novel visible-light-driven photocatalysts based on graphitic carbon nitride. J Colloid Interf Sci 465:83–92

[39] Vignesha K, Suganthi A, Min BK, Kang M (2014) Photocatalytic activity of magnetically recoverable $MnFe_2O_4/g-C_3N_4/TiO_2$ nanocomposite under simulated solar light irradiation. J Mol Catal A: Chem 395:373–383

[40] Akhundi A, Habibi-Yangjeh A (2016) Novel $g-C_3N_4/Ag_2SO_4$ nanocomposites: fast microwave-assisted preparation

and enhanced photocatalytic performance towards degradation of organic pollutants under visible light. J Colloid Interface Sci 482:165–174

[41] He YM, Zhang LH, Fan MH, Wang XX, Walbridge ML, Nong QY, Wu Y, Zhao LH (2015) Z-scheme SnO_{2-x}/g-C_3N_4 composite as an efficient photocatalyst for dye degradation and photocatalytic CO_2 reduction. Sol Energ Mat Sol C 137:175–184

[42] Zhou DT, Chen Z, Yang Q, Shen C, Tang G, Zhao SL, Zhang JJ, Chen D, Wei QH, Dong XP (2016) Facile construction of g-C_3N_4 nanosheets/TiO_2 nanotube arrays as Z-scheme photocatalyst with enhanced visible-light performance. ChemCatChem 6:3064–3073

[43] Li TT, Zhao LH, He YM, Cai J, Luo MF, Lin JJ (2013) Synthesis of g-C_3N_4/$SmVO_4$ composite photocatalyst with improved visible light photocatalytic activities in RhB degradation. Appl Catal B: Environ 129:255–263

[44] Huang LY, Li YP, Xu H, Xu YG, Xia JX, Wang K, Li HM, Cheng XN (2013) Synthesis and characterization of CeO_2/g-C_3N_4 composites with enhanced visible-light photocatalytic activity. RSC Adv 3:22269–22279

[45] Yan SC, Li ZS, Zou ZG (2009) Photodegradation performance of g-C_3N_4 fabricated by directly heating melamine. Langmuir 25:10397–10401

[46] Li GQ, Yang N, Wang WL, Zhang WF (2009) Synthesis, photophysical and photocatalytic properties of N-doped sodium niobate sensitized by carbon nitride. J Phys Chem C 113:14829–14833

[47] Yan LS, Zhang J, Zhou XM, Wu XX, Lan JY, Wang YS, Liu G, Yu JG, Zhi LJ (2013) Crystalline phase-dependent photocatalytic water splitting for hydrogen generation on $KNbO_3$ submicro-crystals. Int J Hydrogen Energy 38:3554–3561

[48] Yan HJ, Chen Y, Xu SM (2012) Synthesis of graphitic carbon nitride by directly heating sulfuric acid treated melamine for enhanced photocatalytic H_2 production from water under visible light. Inter J Hydrogen Energy 37:125–133

[49] Xiang QJ, Yu JG, Jaroniec M (2011) Preparation and enhanced visible-Light photocatalytic H_2-production activity of graphene/C_3N_4 composites. J Phys Chem C 115:7355–7363

[50] Yu HT, Quan X, Chen S, Zhao HM, Zhang YB (2008) TiO_2– carbon nanotube heterojunction arrays with a controllable thickness of TiO_2 layer and their first application in photocatalysis. J Photochem Photobiol A: Chem 200:301–306

[51] Dong F, Zhao ZW, Xiong T, Ni ZL, Zhang WD, Sun YJ, Ho WK (2013) In situ construction of g-C_3N_4/g-C_3N_4 metal-free heterojunction for enhanced visible-light photocatalysis. ACS Appl Mater Interfaces 5:11392–11401

[52] Zong XH, Yan J, Wu GP, Ma GJ, Wen FY, Wang L, Li C (2008) Enhancement of photocatalytic H_2 evolution on CdS by loading MoS_2 as cocatalyst under visible light irradiation. J Am Chem Soc 130:7176–7177

[53] Xu TG, Zhang LW, Cheng HY, Zhu YF (2011) Significantly enhanced photocatalytic performance of ZnO via graphene hybridization and the mechanism study. Appl Catal B: Environ 101:382–387

[54] Han ZZ, Ren LL, Luo M, Chen L, Pan HB, Li CY, Chen JH, Lan JM (2016) In situ synthesis and visible-light photocatalytic application of CdTeSe@TiO_2 nanotube composites with high electron transfer rate. J Mol Catal A: Chem 425:229–236

[55] Zhao ZH, Wang M, Yang TZ, Fang MH, Zhang LN, Zhu HK, Tang C, Huang ZH (2016) In situ co-precipitation for the synthesis of an Ag/AgBr/Bi_5O_7I heterojunction for enhanced visible-light photocatalysis. J Mol Catal A: Chem 424:8–16

[56] Wu YF, Zhang X, Zhang GH, Guan WS (2013) Visible light-assisted synthesis of Pt/Bi_2WO_6 and photocatalytic activity for ciprofloxacin. Micro Nano Lett 9:119–122

[57] Kudo A, Miseki Y (2009) Heterogeneous photocatalyst materials for water splitting. Chem Soc Rev 38:253–278

[58] Martin DJ, Qiu K, Shevlin SA, Handoko AD, Chen XW, Guo ZX, Tang JW (2014) Highly efficient photocatalytic H_2 evolution from water using visible light and structure-controlled graphitic carbon nitride. Angew Chem Int Ed 53:9240–9245

[59] Xu CB, Yang WS, Guo Q, Dai DX, Chen MD, Yang XM (2014) Molecular hydrogen formation from photocatalysis of methanol on anatase-TiO_2(101). J Am Chem Soc 136:602–605

[60] He YM, Zhang LH, Fan MH, Wang XX, Walbridge ML, Nong QY, Wu Y, Zhao LH (2015) Z-scheme SnO_{2-x}/g-C_3N_4 composite as an efficient photocatalyst for dye degradation and photocatalytic CO_2 reduction. Sol Energy Mat Sol C 137:175–184

[61] Cui M, Nong QY, Yu JX, Lin HJ, Wu Y, Jiang XL, Liu XZ, He YM (2016) Preparation, characterization, and photocatalytic activity of CdV_2O_6 nanorods decorated g-C_3N_4 composite. J Mol Catal A: Chem 423:240–247